Electroreduction of low concentration CO_2 at atomically dispersed Ni-N-C catalysts with nanoconfined ionic liquids

Qian Sun [a], Yong Zhao [a], Wenhao Ren [a], Chuan Zhao [a,b,*]

[a] School of Chemistry, The University of New South Wales, Sydney, NSW 2052, Australia
[b] Materials and Manufacturing Futures Institute, The University of New South Wales, Sydney, NSW 2052, Australia

ARTICLE INFO

ABSTRACT

Most studies on electrochemical CO_2 reduction reaction use pure CO_2, which requires extra energy for CO_2 capture and enrichment from atmosphere. Herein, nanoconfined ionic liquids are introduced into porous atomically dispersed nickel-nitrogen-carbon (Ni-N-C) catalysts to enrich local CO_2 concentration and increase the CO_2RR kinetics. A series of high-CO_2-solubility ionic liquids (ILs) were impregnated into the pores of the columnar Ni-N-C catalyst to alter the CO_2-Ni sites interactions and create a solid/liquid interface with high CO_2 concentration. The optimal Ni-N-C/[Bmim][PF$_6$] composite outperforms the Ni-N-C catalyst for pure CO_2 electroreduction with a maximum FE$_{CO}$ of 99.6% and 2.7-fold larger j_{CO}. The high solubility of CO_2 in ILs compared to aqueous electrolyte enables direct electrolysis of CO_2 at low concentrations. When fed with 5–10% (v/v) CO_2, the Ni-N-C/[Bmim][PF$_6$] composite exhibited up to 1.5-fold higher FE$_{CO}$ and a 68% increase of j_{CO}, in comparison to Ni-N-C, and robust stability over 30 h.

1. Introduction

Electrochemical CO_2 reduction reaction (CO_2RR) is a promising technology to reduce CO_2 emissions by converting CO_2 into valuable chemicals, thus mitigating society's dependence on fossil fuels [1,2]. However, CO_2RR is suffering from stable C$=$O bonds (806 kJ/mol) in linear CO_2 molecules [3], and the large reorganizational energy (-1.9 V vs. standard hydrogen electrode) required for transforming linear CO_2 into bent $CO_2^{\bullet-}$ during the first single electron transfer, which imposes slow reaction kinetics and high overpotential for CO_2RR [4]. Other challenges include low CO_2 solubility in aqueous electrolytes [2] and strong competition from hydrogen evolution reaction (HER) [5]. The development of efficient electrocatalysts holds the key to address these challenges [6–14]. Single-atom catalysts (SACs) with homogeneous distribution of well-defined metal active sites on the supports have shown great promises for CO_2RR due to their strong atoms-supports interactions, maximum metal utilization and excellent catalytic activity [15–19]. For example, SACs with metal-nitrogen moieties (M-N$_x$) such as Ni-N SACs have been highly active and selective to CO formation [20,21]. Nonetheless, SACs are generally limited by their single active sites and simple structures, which make it challenging to catalyze complicated reactions involving multiple intermediates such as CO_2RR.

New strategies are needed to functionalize SACs to achieve multi-active sites and/or multi-functionalities.

Up to date, most CO_2RR studies have been using pure CO_2 gas to achieve high electrochemical performances [22–24]. However, industrial CO_2 sources are typically at low concentrations such as that from the fired power plants (5–10% v/v) [25]. Therefore, CO_2 needs to be captured, enriched, and purified to be applied for CO_2RR, which takes a lot of energy and additional cost [26,27]. The direct reduction of low concentration CO_2 is therefore more favorable from an economic prospective [28–30]. ILs have been reported as attractive media for CO_2 capture and electrochemical reduction, attributed to their high CO_2 solubility [31–33], enhanced CO_2 transfer [34], and improved selectivity [35]. Recently, ILs electrolytes have been used for CO_2-to-CO conversion for diluted CO_2 feed, which was demonstrated to be more profitable and economically attractive than using pure CO_2 [27]. However, using ILs electrolytes directly in CO_2 electrolysers generally suffer from several intrinsic limitations of ILs including high viscosity and poor ionic conductivity [36–38], which subsequently lead to sluggish mass transfer and high energy consumption. Additionally, ionic liquids are relatively costly. Therefore, using large quantity of viscous ILs in CO_2 electrolysers for CO_2 capture and reduction is technologically and economically impractical.

Herein, we show an atomically dispersed Ni-N-C catalyst with nanoconfined ILs for efficient CO_2RR in both pure and low concentration CO_2. The nanoconfined ILs play multiple roles as a CO_2 concentrator, a co-catalyst, and a HER suppressor. Using ILs confined in nanoscale pores also solves the high viscosity and low conductivity issues that bulk IL electrolytes have for CO_2RR [36–38]. A series of ILs with different combinations of cations and anions were employed and their effects on CO_2RR are studied. The optimized Ni-N-C/[Bmim][PF$_6$] composite exhibited promising catalytic performances for electroreduction of CO_2 at low concentration, demonstrating great potentials of the Ni-N-C/ILs composites for future industrial CO_2 electroreduction applications.

2. Experimental section

2.1. Chemicals

Nickel(II) nitrate was purchased from Chem-Supply Pty. Ltd. Melamine was purchased from Sigma-Aldrich Pty Ltd. 1-butyl-3-methylimidazolium tetrafluoroborate ([Bmim][BF$_4$]), 1-ethyl-3-methylimidazolium triflate ([Emim][CF$_3$SO$_3$]), 1-ethyl-3-methylimidazolium tetrafluoroborate ([Emim][BF$_4$]), 1-ethyl-3-methylimidazolium bis(trifluoromethylsulfonyl)imide ([Emim][TF$_2$N]), and 1-butyl-3-methylpyridinium bis(trifluoromethylsulfonyl)imide ([BMPy][TF$_2$N]) were purchased from IoLiTec Ionic Liquids Technologies. 1-butyl-3-methylimidazolium hexafluorophosphate ([Bmim][PF$_6$]), and methanol were purchased from Chem-Supply Pty. Ltd. 1–butyl-3–methylimidazolium trifluoromethanesulfonate ([Bmim][CF$_3$SO$_3$]) was purchased from Sigma-Aldrich Pty Ltd. All reagents and solvents were of analytical grade and used as received without additional purification. The CO_2 and Ar feed gases were purchased from Air Liquide in Australia.

2.2. Preparation of Ni-N-C

In a typical procedure, Nickel(II) nitrate and melamine were mixed together with a mass ratio of 1:10, other mass ratios don't exhibit significant difference in CO_2RR performances (Fig. S1), then annealed at high temperature (1000 °C) under Ar flow. After which, the obtained black powders were washed with HCl, centrifuged, washed with distilled water several times and dried in vacuum at 60 °C overnight, obtaining the columnar Ni-N-C. During the pyrolysis of Ni^{2+} and melamine, melamine was gradually converted to g-C$_3$N$_4$ via poly-condensation at 370–600 °C [23]. Meanwhile, the Ni atoms were immobilized onto the defect sites of g-C$_3$N$_4$. With increasing the temperature over 700 °C, the carbon growth was catalyzed by the immobilized Ni atoms. The in situ formed g-C$_3$N$_4$ as the template guided the formation of atomically dispersed Ni-N-C catalyst.

2.3. Preparation of Ni-N-C/ILs composite catalysts

To prepare the Ni-N-C/ILs composite catalysts, ILs were confined in Ni-N-C catalyst using a simple ultrasonication-centrifugation method. The Ni-N-C catalyst powder (80 mg) was homogeneously dispersed in 4 mL ILs ([Bmim][BF$_4$], [Bmim][PF$_6$], [Emim][TF$_2$N], [BMPy][TF$_2$N], [Bmim][CF$_3$SO$_3$], [Emim][CF$_3$SO$_3$], [Emim][BF$_4$]) under ultrasonication for 1 h at room temperature. Subsequently, the slurry was centrifuged, washed with methanol once to remove the ILs on the outer surface of the Ni-N-C catalyst, and then dried in vacuum at 70 °C overnight, obtaining the Ni-N-C/ILs. The Ni-N-C/ILs composite catalysts prepared from various ILs were denoted as Ni-N-C/[Bmim][BF$_4$], Ni-N-C/[Bmim][PF$_6$], Ni-N-C/[Emim][TF$_2$N], Ni-N-C/[BMPy][TF$_2$N], Ni-N-C/[Bmim][CF$_3$SO$_3$], Ni-N-C/[Emim][CF$_3$SO$_3$], and Ni-N-C/[Emim][BF$_4$].

2.4. Catalyst characterizations

Scanning electron microscope (SEM) images were collected using QUANTA 450. Transmission electron microscopy (TEM), high angle annular dark-field scanning TEM (HAADF-STEM), and energy-dispersive X-ray spectroscopy (EDS) mapping images were obtained by JEOL JEMARM200f microscope at 200 kV. X-ray spectroscopy (XPS) results were obtained by Thermo ESCALAB250i. X-ray diffraction (XRD) was carried out on a PANalytical X′Pert X-ray diffraction system (45 kV, 40 mA, Cu Kα radiation). Brunauer-Emmett-Teller (BET) surface areas were measured using Tristar II 3020 instrument by nitrogen adsorption at 77 K. Fourier transform infrared (FT-IR) spectra was collected by Spectrum 100/Spotlight 400. Nuclear Magnetic Resonance (NMR) was conducted using Bruker Advance III 400 (Rabi).

2.5. Electrochemical measurements

CO_2RR measurements were conducted in a H-cell which consisted of a reference electrode (saturated calomel electrode, SCE), a Pt wire counter electrode and a working electrode separated by Nafion membrane. 10 mg catalysts were dispersed into the solution of H$_2$O (100 μL), ethanol (300 μL), and 5 wt% Nafion solution (100 μL), which were sonicated for 2 h at room temperature. Then, the ink was dropped onto carbon fiber paper and dried in air, obtaining the working electrode with 1 mg/cm^2 catalyst loading. The electrochemical data were collected in 0.5 M KHCO$_3$. The potentials were calculated by the Nernst equation (E$_{RHE}$ = E$_{SCE}$ + 0.0591 × pH + 0.241 V, 25 °C).

Chronoamperometry was employed to measure the products and Faradic efficiency of CO_2RR at fixed potentials. The gaseous products were quantified using a gas chromatograph (GC) equipped with a flame ionization detector (FID) for CO and CH$_4$ and a thermal conductivity detector (TCD) for H$_2$ quantification. The carrier gas was ultrapure Ar (99.999%). The CO_2 flow rate was 20 sccm controlled by a Cole-Parmer mass flow meter for electroreduction of pure CO_2. While for diluted CO_2 reduction, flow rate ratio of CO_2/(Ar+CO_2) was adjusted to give 5%, 10%, 25%, and 50% CO_2 concentration. GC was calibrated using standard gas mixtures under standard conditions (1 atm, 298 K, Fig. S2).

According to the definition of faradaic efficiency (FE):

$$FE = \frac{\alpha \times F \times n}{Q} = \frac{\alpha \times F \times n}{I_{total} \times t}$$

And ideal gas law:

$$P \times V = n \times R \times T \rightarrow n = \frac{P_o \times V_{volume} \times r}{R \times T_0}$$

Therefore, the FE can be written as:

$$FE = \frac{\alpha \times F}{I_{total}} \times \frac{P_o \times r}{R \times T_0} \times \frac{V_{volume}}{t} = \frac{\alpha \times F \times P_o \times r \times V_{flow\ rate}}{R \times T_0 \times I_{total}}$$

Where, α: the number of electrons transferred during reaction (α$_{CO}$ = α$_{H2}$= 2); F: Faradaic constant (96,485 C/mol); P$_0$: atmospheric pressure (101,325 N/m^2); r: gas concentration (ppm), r$_{CO}$ = 0.000110118A$_{CO}$, r$_{H2}$ = 0.00312A$_{H2}$; V$_{flow\ rate}$: CO_2 volumetric flow rate (sccm); R: ideal gas constant (8.314 N m/(mol K)); T$_0$: reaction temperature (298.15 K); I$_{total}$: total current (A). Therefore, FE$_{CO}$ and FE$_{H2}$ were calculated as the following:

$$FE_{CO} = \frac{0.1315 \times V_{flow\ rate} \times (0.000110118A_{CO})}{I_{total}} \times 100\%$$

$$FE_{H2} = \frac{0.1315 \times V_{flow\ rate} \times (0.00312A_{H2})}{I_{total}} \times 100\%$$

Where, A$_{CO}$: integral area of CO peak tested by GC; A$_{H2}$: integral area of H$_2$ peak tested by GC.

2.6. Electrochemical active surface areas (ECSA) measurements

The ECSA is proportional to double-layer capacitance (C_{dl}) values. C_{dl} was determined in H-type cell by measuring the capacitive current associated with double-layer charging from the scan-rate dependence of cyclic voltammetry (CV). The CV ranged from -0.5 to -0.6 V vs SCE. The scan rates were 10, 20, 40, 60, 80 and 100 mV/s. C_{dl} was estimated by plotting the anodic and cathodic current density difference at -0.55 V vs SCE against the scan rates.

ECSA was calculated based on the definition:

$$ECSA = C_{dl}/C_s$$

Where C_{dl} corresponds to the slope of the double-layer charging current vs the scan rate plot, and the value of C_s we used is 40 µF/cm^2.

3. Results and discussions

3.1. Preparation and characterization of Ni-N-C/ILs composite catalysts

The Ni-N-C catalyst with nanoconfined ILs were fabricated using a facile impregnation method (Fig. 1a). Firstly, Ni-N-C catalyst was prepared by calcinating a solid mixture of Ni^{2+} and melamine at high temperature to yield a porous columnar carbon structure with uniformly distributed Ni atoms. The Ni-N-C catalyst powder was then dispersed in ILs under ultrasonication at room temperature. ILs were easily confined into the pores of Ni-N-C catalyst by capillary force. The sample was then centrifuged, washed with methanol to remove the ILs adsorbed on the outer surface of the Ni-N-C catalyst, and then dried in vacuum to obtain the Ni-N-C/ILs composite. To systematically investigate the effects of nanoconfined ILs for CO_2RR, we deployed a series of ILs with different combinations of cations and anions, i.e., [Bmim][BF$_4$], [Bmim][PF$_6$], [Emim][TF$_2$N], [BMPy][TF$_2$N], [Bmim][CF$_3$SO$_3$], [Emim][CF$_3$SO$_3$], [Emim][BF$_4$] (Fig. S3, Table S1).

SEM (Fig. 1b) and TEM (Fig. 1d) images revealed that the Ni-N-C/[Bmim][PF$_6$] composite presented a columnar morphology with abundant pores, and exhibited isolated Ni atoms on carbon support, shown as the bright spots in the HAADF-STEM picture (Fig. 1c). Similar results were observed for the Ni-N-C catalyst (Fig. S4a–b). Ni nanoparticles were also detected, which appear as the dark parts in the HAADF-STEM (Figs. S4c, S5). Moreover, the energy-dispersive X-ray spectroscopy
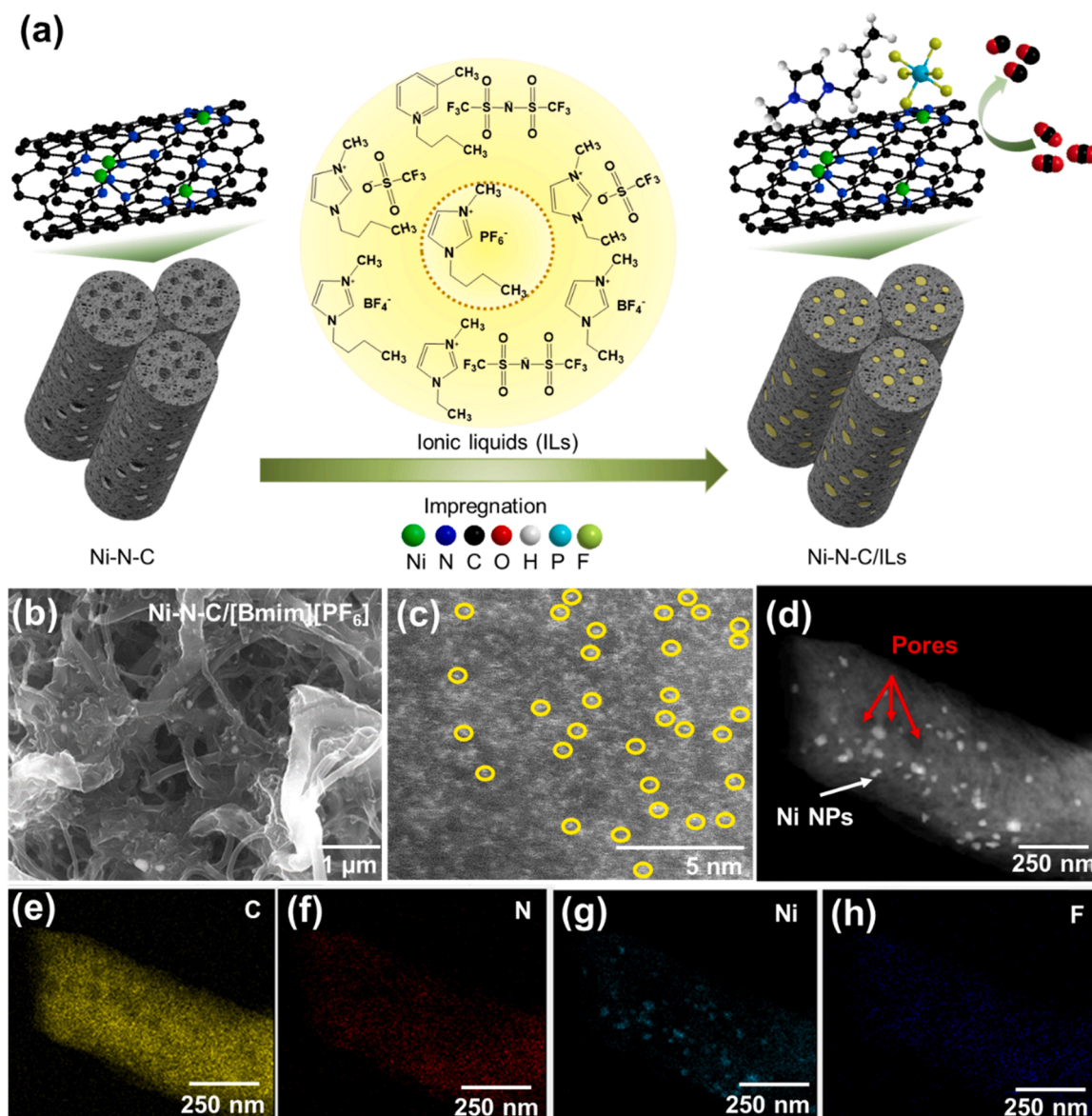

Fig. 1. Synthesis and structural characterization. (a) Preparation of Ni-N-C/[Bmim][PF$_6$] composite catalysts. (b) SEM of Ni-N-C/[Bmim][PF$_6$]. (c) HAADF-STEM of Ni single atoms in Ni-N-C/[Bmim][PF$_6$]. (e-h) EDS mapping of Ni-N-C/[Bmim][PF$_6$] for (d).

(EDS) suggested homogeneous dispersion of C, N, Ni from the Ni-N-C host and F from the ILs (Figs. 1e-h, S4d–g).

As shown in the X-ray diffraction (XRD) spectra, the Ni-N-C catalyst and Ni-N-C/ILs composites exhibited similar carbon peaks at 26.5°, 44.6°, 74.2° for (002), (101), (112) planes, and two nickel peaks for (111) and (200) planes attributed to the Ni nanoparticles (Fig. 2a, S6). X-ray photoelectron spectroscopy (XPS) was performed to analyze the element state of catalyst surface and composition. The Ni 2p XPS spectrum of Ni-N-C and Ni-N-C/[Bmim][PF$_6$] was dominated by the peak at 854.8 eV (Fig. S7a), which was lower than the Ni^{2+} (856 eV) in nickel phthalocyanine (NiPc) [39], assigning to the low-valent Ni$^{\delta+}$ in the catalysts. Besides, the N 1s spectra indicated the presence of pyridinic N (398.92 eV), Ni-N (400.05 eV), pyrrolic N (401.25 eV) and graphitic N (404.53 eV) in the Ni-N-C and Ni-N-C/[Bmim][PF$_6$] samples (Fig. S7b). Fourier transform infrared (FT-IR) spectra for the Ni-N-C/[Bmim][PF$_6$] sample shows the characteristic vibration of methine (C-H) in [Bmim]$^+$ (3172, 1386, 1169, 748 cm^{-1}), stretching vibration of [PF$_6$]$^-$ (842 cm^{-1}) and the C-N vibration inside [Bmim][PF$_6$] (1574 cm^{-1}) [40, 41], suggesting the successful introduction of ILs into the Ni-N-C catalyst (Figs. 2c, S8).

Brunauer-Emmett-Teller measurements were performed to investigate the specific surface area and pore size distribution of the samples. The Ni-N-C catalyst showed a surface area of 123 m^2/g with mesopores at 2.3–21.6 nm (Fig. 2b, S9). The Ni-N-C/[Bmim][PF$_6$] composite exhibited lower surface area (66 m^2/g) and mesopores (2.5–11.0 nm), indicating the successful impregnation of [Bmim][PF$_6$] into the interior pores of the Ni-N-C host. To estimate the ILs content in the composite,

the masses of the catalysts before and after introducing nanoconfined ILs were denoted as m$_1$ and m$_2$, respectively. The estimated ILs contents were calculated by the ratio of (m$_2$-m$_1$)/m$_2$. The Ni-N-C/[Bmim][PF$_6$] composite delivered a relatively large IL content (45.58 wt%, Table S2), favorable to improving the CO$_2$ concentration in aqueous electrolyte. Furthermore, electrochemical active surface area (ECSA), estimated from the double-layer capacitance (Figs. S10–S11a) [42], also showed that the Ni-N-C/[Bmim][PF$_6$] composite has a lower ECSA value than the Ni-N-C catalyst (Fig. S11b) due to the blocked pores in the Ni-N-C by [Bmim][PF$_6$] impregnation.

3.2. Electroreduction of pure CO$_2$ using Ni-N-C/ILs composite catalysts

CO$_2$RR measurements were carried out in a three-electrode H-cell using CO$_2$-saturated 0.5 M KHCO$_3$ as the electrolyte (Fig. S12). In this work, all samples were washed by 3 M HCl to remove the Ni nanoparticles outside the carbon nanotube. The remained Ni nanoparticles were wrapped inside the carbon nanotube which do not directly participate in the CO$_2$ electroreduction [43,44]. The excellent performances of Ni-N-C/[Bmim][PF$_6$] on CO$_2$ electroreduction was therefore attributed to atomically dispersed Ni sites (Figs. 3 a, b, 4). To further confirm this and elucidate the role of Ni nanoparticles (NPs), the control experiment was performed. Two Ni-N-C samples were prepared with and without acid washing, which were denoted as Ni-N-C (acid washing) and Ni-N-C (no acid washing), respectively. According to the SEM images (Fig. S13a–b), Ni-N-C (acid washing) presented clear carbon nanotube structure and few Ni NPs on the surface of carbon nanotubes,
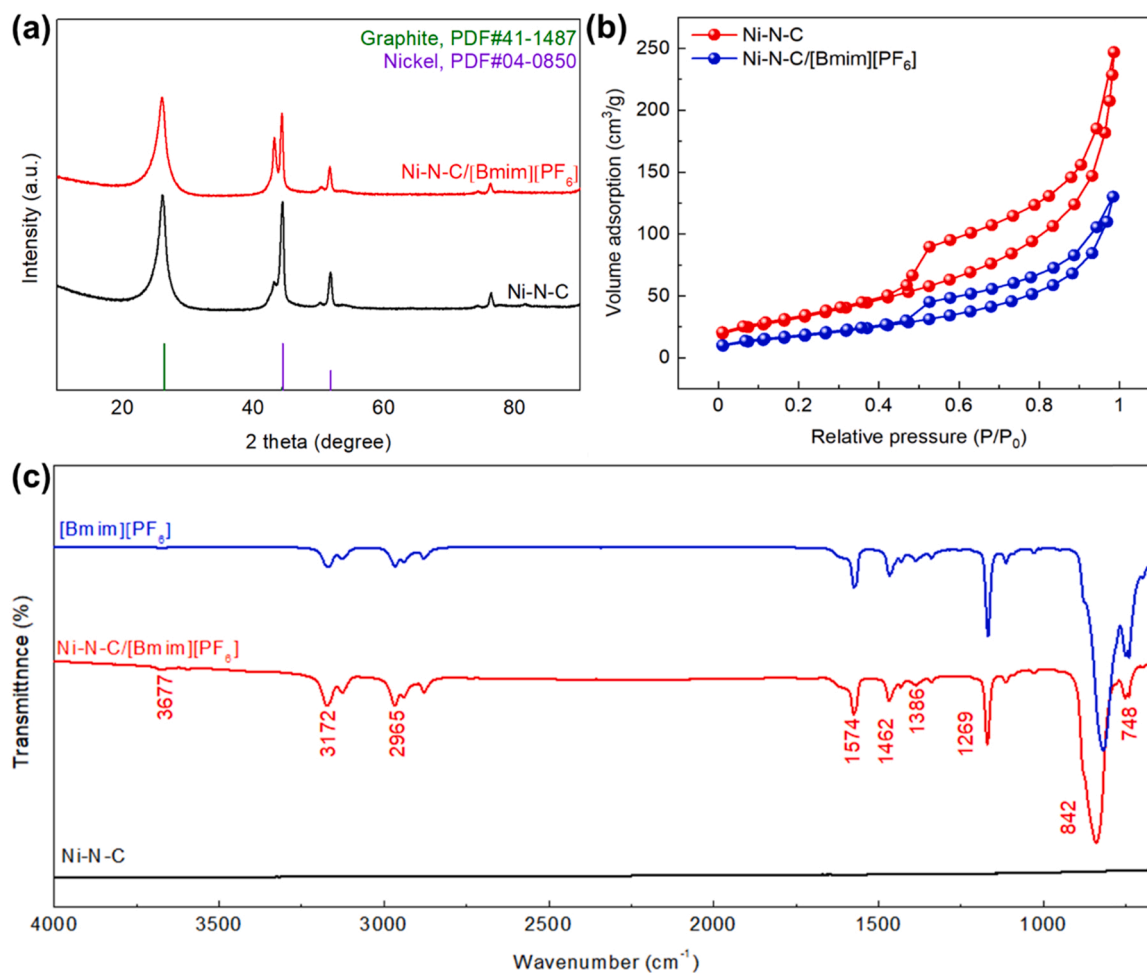

Fig. 2. (a) XRD of Ni-N-C catalyst and Ni-N-C/[Bmim][PF$_6$] composite catalysts. (b) Nitrogen adsorption-desorption isotherms for Ni-N-C, and Ni-N-C/[Bmim][PF$_6$]. (c) IR of Ni-N-C, Ni-N-C/[Bmim][PF$_6$], and pure [Bmim][PF$_6$].
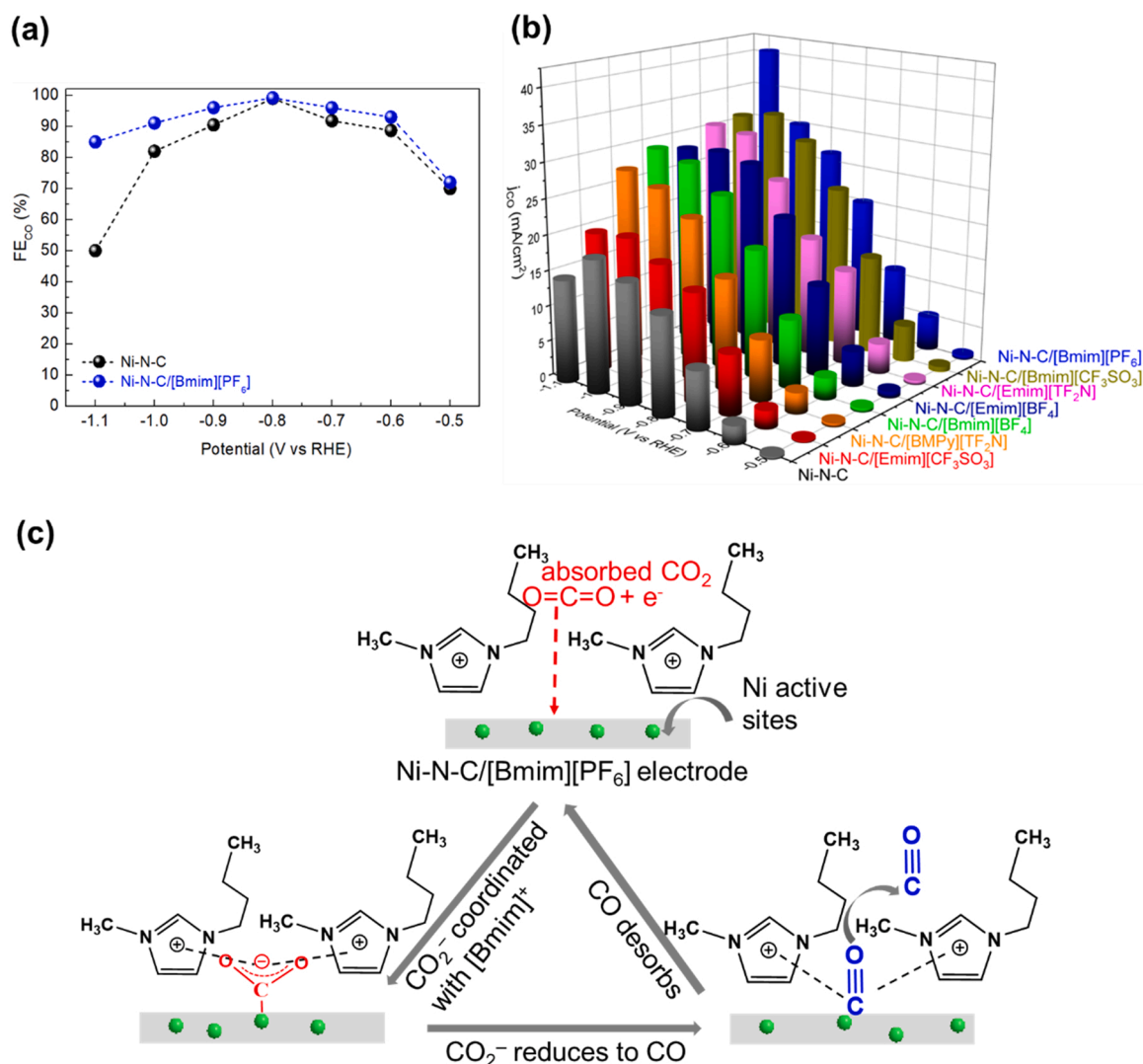
Fig. 3. (a) FE_{CO} of Ni-N-C catalyst and Ni-N-C/[Bmim][PF_6]. (b) j_{CO} of Ni-N-C catalyst and Ni-N-C/ILs composite catalysts. (c) Mechanism of CO_2RR on Ni-N-C/[Bmim][PF_6] electrodes.

while Ni-N-C (no acid washing) exhibited abundant Ni NPs on the surface. XRD results revealed stronger Ni NPs peaks of Ni-N-C (no acid washing) than that of Ni-N-C (acid washing), the larger intensity ratio of Ni NPs peak to carbon peak (Ni(111)/C(002)) for Ni-N-C (no acid washing) verified more Ni NPs on carbon nanotube (Fig. S13c). However, the Ni-N-C (acid washing) and Ni-N-C (no acid washing) presented similar CO_2RR performance (Fig. S14), which demonstrated that Ni NPs do not contribute significantly to CO_2RR. This is consistent with previous studies that Ni NPs don't present significant activity for CO_2RR [43, 44].

It is found that all Ni-N-C/ILs composites outperform the Ni-N-C catalyst over a wide potential range from −0.5 V to −1.1 V vs RHE, delivering higher FE_{CO} (Figs. 3a, S15a), lower Faradaic efficiency of H_2 (FE_{H2}, Fig. S15b), and larger CO partial current density (j_{CO} per geometric area, Fig. 3b). Among various Ni-N-C/ILs composites, Ni-N-C/[Bmim][PF_6] reached a maximum FE_{CO} of 99.6% at −0.8 V vs RHE, slightly higher than that of Ni-N-C catalyst (98.8%). Notably, at more negative potential of −1.1 V vs RHE, it also exhibited high FE_{CO} of 85.0% and maximum j_{CO} of 40.0 mA/cm², which were 1.7- and 2.7-fold higher than that of Ni-N-C at same applied potential, respectively, which meant higher selectivity to CO than HER by the nanoconfined [Bmim][PF_6]. This indicated the effects of the nanoconfined [Bmim][PF_6] in suppressing H_2 and offering higher selectivity to CO at high applied

potential. Besides, the nanoconfined [Bmim][PF_6] into Ni-N-C catalyst also contributed to better CO_2RR performance than some other efficient catalysts using electrolytes of ILs as summarized in Table S4. Additionally, the CO partial current density normalized by ECSA (j_{CO} per ECSA, Fig. S15c) for the Ni-N-C/ILs is also larger than that of Ni-N-C catalyst, suggesting the intrinsic activity of each active site of Ni-N-C catalyst is enhanced for CO_2RR upon ILs confinement, rather than a simple surface area effect. The surface area effect normally means the larger surface area, the more active sites, and the higher electrochemical performance. However, in our system the Ni-N-C/[Bmim][PF_6] exhibited a lower surface area but better electrochemical performances than the Ni-N-C catalyst. Therefore, the enhanced electrochemical performances are not purely originated from enlarged surface area but also the ionic liquid co-catalysis effect. Nyquist plots (Fig. S16) were conducted to study the ohmic resistance of system (Rs) and mass transfer property of catalysts. In the bulk [Bmim][PF_6] electrolyte, large Rs (∼211.08 Ω) and diffusion coefficient (slopes at low-frequency) deteriorated significantly because of the high viscosity (310 mPa·s) of ILs [37,45]. While in 0.5 M $KHCO_3$ aqueous electrolyte, Ni-N-C/ILs and Ni-N-C showed small Rs (1.77–10.31 Ω) at high-frequency region (Table S3) and similar slopes at low-frequency region, demonstrating the ILs confinement has negligible effect on the electronic conductivity and the system diffusivity. This can also be elucidated by the Bode plots (Fig. S17) where two
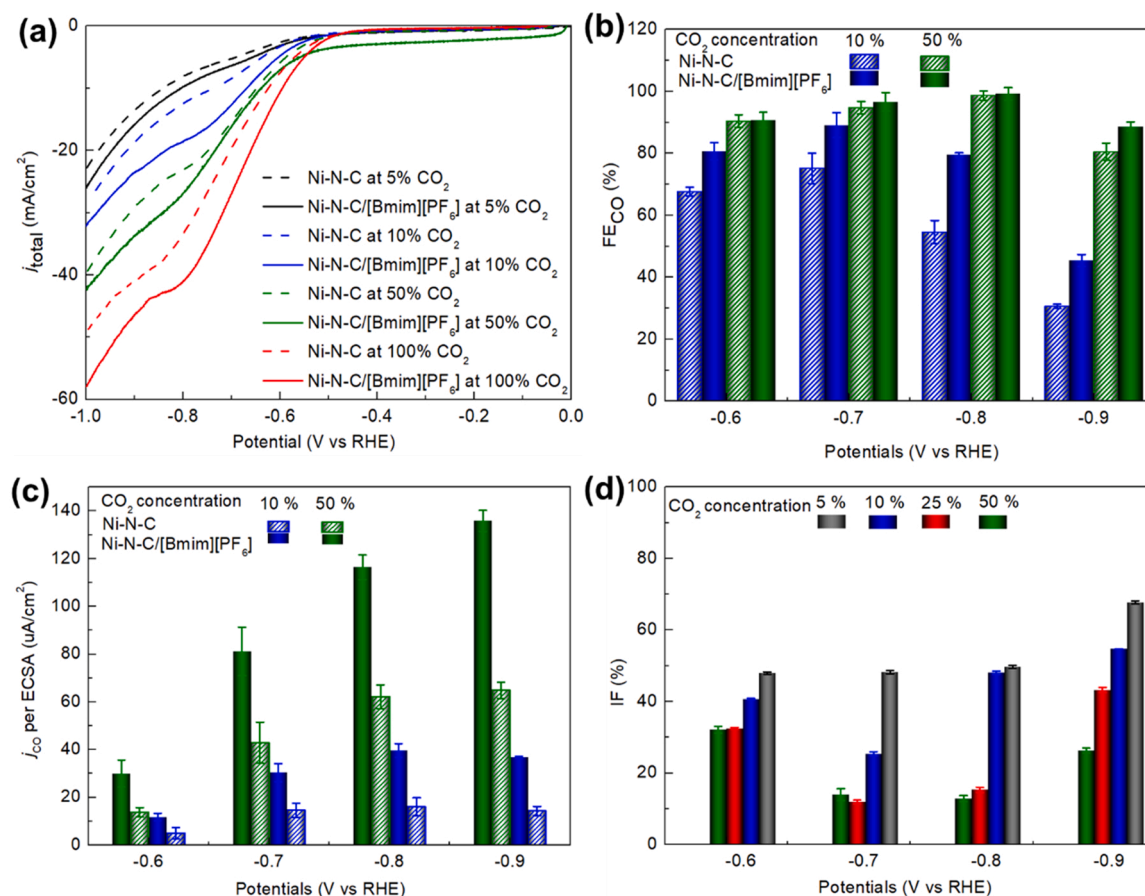
Fig. 4. Electrochemical performances of Ni-N-C/[Bmim][PF$_6$] for electroreduction of diluted CO$_2$. (a) LSV curves in diluted CO$_2$ (5%, 10%, 50%) and pure CO$_2$. (b) FE$_{CO}$ of Ni-N-C and Ni-N-C/[Bmim][PF$_6$] in 10% and 50% CO$_2$. (c) j_{CO} per ECSA of Ni-N-C and Ni-N-C/[Bmim][PF$_6$] in 10% and 50% CO$_2$. (d) IF values for Ni-N-C/[Bmim][PF$_6$] based on Ni-N-C in 5%, 10%, 25%, and 50% CO$_2$ concentrations at different applied potentials. Error bars indicate the standard deviation of three independent samples.
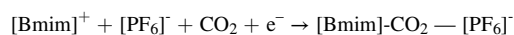
slopes (two time-constants upon decreasing frequency) for the kinetic and diffusion process were observed, respectively. Both Ni-N-C/ILs and Ni-N-C samples displayed similar slopes for the kinetic process at higher frequency, while slightly higher slopes of the diffusion process of the Ni-N-C/ILs were detected. The peaks at lower frequency regions were featured by the charge transfer to Faradic adsorbed CO$_2$ reduction intermediates on the electrode surface. All these indicated similar charge transfer kinetics of Ni-N-C/ILs and Ni-N-C, signifying the negligible effects of the ILs modifications on the conductivity and diffusivity.
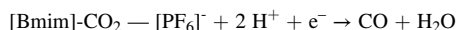
To understand the effects of IL structures on CO$_2$RR activity, j_{CO} values of the Ni-N-C/ILs composites with different IL anions or cations were compared. It was found the j_{CO} values obtained generally follow the trend of CO$_2$ solubilities in different ILs. For example, using the ILs with same anions such as [CF$_3$SO$_3$]$^-$ and [BF$_4$]$^-$, the j_{CO} values follow the order of Ni-N-C/[Bmim][CF$_3$SO$_3$] > Ni-N-C/[Emim][CF$_3$SO$_3$] > Ni-N-C (Fig. S18) and Ni-N-C/[Bmim][BF$_4$] > Ni-N-C/[Emim][BF$_4$] > Ni-N-C (Fig. S19). The longer chain lengths of the imidazolium cations (e.g. [Bmim]$^+$ vs [Emim]$^+$) is reported to result in the higher CO$_2$ solubility [46]. For the ILs with same cations such as [Bmim]$^+$ and [Emim]$^+$, the following j_{CO} orders of Ni-N-C/[Bmim][PF$_6$] > Ni-N-C/[Bmim][BF$_4$] > Ni-N-C (Fig. S20) and Ni-N-C/[Emim][Tf$_2$N] > Ni-N-C/[Emim][BF$_4$] > Ni-N-C have been found (Fig. S21), which also broadly follow the CO$_2$ solubility trends in the ILs (Table S1) [38,47].

However, CO$_2$ solubility is found not the only factor that determines the catalytic activity of the Ni-N-C/ILs. Other factors contribute as well. For example, the CO$_2$ solubility in [Bmim][PF$_6$] and [Emim][Tf$_2$N] is lower than that in [BMpy][Tf$_2$N] (Table S1). However, the Ni-N-C/[Bmim][PF$_6$] and Ni-N-C/[Emim][Tf$_2$N] composites exhibited higher

activity and j_{CO} than Ni-N-C/[BMpy][Tf$_2$N] (Fig. S22). In this case, the co-catalyst effect of the nanoconfined ILs is believed to play an important role. It has been established that imidazolium-based ILs e.g. [Emim]$^+$ and [Bmim]$^+$ can promote CO$_2$RR by stabilizing the intermediate CO$_2$*$^-$ via the formation of [Emim]-CO$_2$ and [Bmim]-CO$_2$ complex during the CO$_2$RR process (Fig. 3c), increasing the local CO$_2$ concentration near cathode surface, and lowering the energy barrier for CO$_2$ reduction [48,49].

Fig. 3c illustrated the plausible mechanism for the enhancement of electrochemical performance CO$_2$RR by the introduction of the nanoconfined ILs. Normally, during the CO$_2$RR process catalyzed by atomically distributed Ni-N-C catalyst, the surface absorbed CO$_2$ was transformed into COOH* intermediate via a concerted H$^+$/e$^-$ transfer and further reduced to CO via a second H$^+$/e$^-$ transfer, or the *COOH intermediate was generated via a decoupled H$^+$/e$^-$ transfer with the formation of the surface absorbed CO$_2$*$^-$ radical which were the typical CO$_2$RR pathways for CO formation (Fig. S23) [50,51]. With introducing the nanoconfined ILs such as [Bmim][PF$_6$], the [Bmim]$^+$ cations can coordinate with the CO$_2$*$^-$ radicals to form [Bmim]-CO$_2$ complexes, providing a low-energy pathway for CO production [48,49]. This is different from Ni-N-C catalyst where the rate-limiting step of one electron transfer to CO$_2$ form a high-energy intermediate [49]. The [Bmim]-CO$_2$ complex was finally converted to adsorbed CO followed by CO desorption (Fig. 3c). Therefore, the cathodic reaction by Ni-N-C/[Bmim][PF$_6$] was different from that without ILs (2CO$_2$ + 2 H$^+$ + 2e$^-$ → CO + H$_2$O) [48,49,52]. With ILs such as [Bmim][PF$_6$] [49]:

[Bmim]$^+$ + [PF$_6$]$^-$ + CO$_2$ + e$^-$ → [Bmim]-CO$_2$ —— [PF$_6$]$^-$

$$[Bmim]\text{-}CO_2 \longrightarrow [PF_6]^- + 2\,H^+ + e^- \rightarrow CO + H_2O$$

Most ILs, if not all, including both hydrophobic and hydrophilic ILs, have some degree of water miscibility [53]. Therefore, the ILs cannot block the contact of water or ions to the catalyst. Here in our case, even the hydrophobic [Bmim][PF$_6$] still can have a water miscibility up to 2.67 ± 0.03 wt% [54]. Water present in [Bmim][PF$_6$] is in contact with the catalyst surface and act as a proton source. This has been established in previous studies where [Bmim][PF$_6$] is directly as bulk electrolytes for CO_2RR [46,55]. [Bmim][BF$_4$], [Emim][BF$_4$], [Bmim][CF$_3$SO$_3$], and [Emim][CF$_3$SO$_3$] are hydrophilic, [Bmim][PF$_6$], [BMPy][TF$_2$N], and [Emim][TF$_2$N] are hydrophobic ILs. In this work, as hydrophilic ILs can dissolve in aqueous solutions [56,57], hydrophobic ILs are generally preferred as they are more stable in aqueous 0.5 M KHCO$_3$ electrolyte and stably confined into the porous Ni-N-C catalyst, thereby offering a steady electrolysis performance. The hydrophobicity of ILs can be further tuned by altering the combinations of anions and cations. For example, the longer alkyl chain length of the cations, the stronger hydrophobicity. The stronger the hydrogen bonding anions could form (anion…HOH…anion) with water (e.g. [PF$_6$]$^-$ < [TF$_2$N]$^-$ < [BF$_4$]$^-$ < [CF$_3$SO$_3$]$^-$), the more hydrophobic the ionic liquids are [53,58]. In our study, among the ionic liquids applied, the [Bmim][PF$_6$] composite exhibited the best electrochemical performance for CO_2 reduction (Fig. 3b). The nanoconfined [Bmim][PF$_6$] is found quite stable and do not have significant loss during CO_2RR measurement, as confirmed by ^{1}H NMR and ^{13}C NMR (Fig. S24).

3.3. Electroreduction of diluted CO_2

The high solubility of CO_2 in ILs have made them attractive media for CO_2 capture [31–33], which inspired us to explore CO_2 capture and electroreduction at the same Ni-N-C/IL composite catalysts. Thus, diluted CO_2 of 5%, 10%, 25% and 50% (v/v) were prepared by mixing CO_2 with Ar at different flow rate ratios and applied to the electrochemical cell. Ni nanoparticles were not the main factor contributing to the CO_2RR under low CO_2 partial pressure, which was confirmed by the similar electrochemical performances of diluted CO_2 reduction for the Ni-N-C catalysts with and without acid washing (Fig. S25). Ni-N-C/[Bmim][PF$_6$] composite was selected for electroreduction of low concentration CO_2 due to its high activity and selectivity (e.g. j_{CO} and FE$_{CO}$), as a result of its high CO_2 solubility and the co-catalyst effect. As shown in linear sweep voltammetry (LSV, Fig. 4a), the total current density (j_{total}) for both Ni-N-C catalyst and Ni-N-C/[Bmim][PF$_6$] composite increase as expected upon increasing CO_2 concentration from 5% to 100%. In comparison to Ni-N-C, the Ni-N-C/[Bmim][PF$_6$] catalyst always shows larger j_{total} (Fig. 4a), higher FE$_{CO}$ (Figs. 4b, S26), larger j_{CO} per geometric area (Fig. S27) and j_{CO} per ECSA (Figs. 4c, Fig. S28) than the Ni-N-C catalyst, as expected, attributed to the high CO_2 solubility in [Bmim][PF$_6$], the co-catalytic effect, and CO_2 preconcentration by [Bmim][PF$_6$]. For example, at low CO_2 concentrations of 10%, Ni-N-C/[Bmim][PF$_6$] achieved maximum FE$_{CO}$ of 89.1% with j_{CO} of 4.91 mA/cm^2 at -0.7 V vs RHE, which is comparable to other reported effective catalysts for diluted CO_2RR (Table S5).

To further understand the preconcentration effects of [Bmim][PF$_6$] on j_{CO}, the increase factor (IF) of the CO partial current density against Ni-N-C catalyst (IF = $[(j_{CO(Ni\text{-}N\text{-}C/[Bmim][PF6])} - j_{CO(Ni\text{-}N\text{-}C)})/j_{CO(Ni\text{-}N\text{-}C)}]$ × 100%) was determined (Fig. 4d). It was found that larger IF values were always obtained for Ni-N-C/[Bmim][PF$_6$] at lower CO_2 concentrations. For example, when using 50% (v/v) CO_2, IF values of 26%, 13%, 14% and 32% are achieved at -0.9, -0.8, -0.7 and -0.6 V vs RHE, respectively. While at 5% (v/v) CO_2, the j_{CO} with maximum IF values of 68%, 50%, 48%, and 48% were obtained at -0.9, -0.8, -0.7 and -0.6 V vs RHE, respectively. The higher increase factor obtained at lower CO_2 concentration can be attributed to the high solubility and local pre-concentration of CO_2 in [Bmim][PF$_6$]. Additionally, the IF values at different CO_2 concentrations exhibited a decreasing trend with

the potential changing from -0.6 V to -0.7 V vs RHE, then followed by a gradual increase upon more negative potentials from -0.7 V vs -0.9 V vs RHE. This behavior is related to the intrinsic activity of the atomically dispersed Ni-N-C catalyst for CO_2RR which are more active around -0.7 and -0.8 V vs RHE [52,59]. Moreover, stability testing was performed at -0.8 V vs RHE with 10% (v/v) CO_2, a typical CO_2 concentration in the waste gas from fire power plants. The Ni-N-C/[Bmim][PF$_6$] presented stable FE$_{CO}$ and j_{CO} over 30 h continuous CO_2 electrolysis (Fig. S29). Slight difference between the FE$_{CO}$ by stability testing (Fig. S29) and that in 10% CO_2 concentration (Fig. 4b) was likely due to the difference of catalysts form batch to batch, as well as the impregnation process for confinement of ionic liquid.

4. Conclusions

We developed a facile nanoconfined ILs strategy for improving the reduction of low concentration CO_2. Among a series of Ni-N-C/ILs composites, Ni-N-C/[Bmim][PF$_6$] achieved the best catalytic performance for pure CO_2 reduction with maximum FE$_{CO}$ of 99.6% and j_{CO} of 40 mA/cm^2 at -0.8 V and -1.1 V vs RHE, respectively. When applied for diluted CO_2 reduction, Ni-N-C/[Bmim][PF$_6$] exhibited higher FE$_{CO}$ and j_{CO} than the atomically dispersed Ni-N-C catalyst, as well as excellent stability over 30 h under a low concentration of 10%. These excellent performances are attributed to the high CO_2 solubility in ionic liquids, intrinsic activity of single atomic Ni-N-C sites, the large surface area of carbon nanotubes to expose abundant Ni sites, fast electron/mass transfer facilitated by carbon nanotubes, and the co-catalyst effect of the ionic liquid. Because ionic liquids are designable and have been extensively used for CO_2 capture. It is expected that ionic liquids with higher CO_2 solubility and suitable combinations of cations and anions can be designed to further enhance the conversion of low concentrations CO_2 from various industrial sources. The nanoconfined ILs also provide simple yet versatile strategy for tuning the properties of atomically dispersed metal-nitrogen sites for a range of catalytic applications.

CRediT authorship contribution statement

Qian Sun: Conceptualization, Validation, Data curation, Investigation, Formal analysis, Writing – original draft. **Yong Zhao:** Writing – review & editing. **Wenhao Ren:** Writing – review & editing. **Chuan Zhao:** Writing – review & editing, Supervision, Funding acquisition.

Declaration of Competing Interest

The authors declare that they have no known competing financial interests or personal relationships that could have appeared to influence the work reported in this paper.

Acknowledgements

Appendix A. Supporting information

Supplementary data associated with this article can be found in the online version at doi:10.1016/j.apcatb.2021.120963.

References

[1] C.Z. Zhu, S.F. Fu, Q.R. Shi, D. Du, Y.H. Lin, Single-atom electrocatalysts, Angew. Chem. Int. Ed. 56 (2017) 13944–13960.

[2] K. Jiang, S. Siahrostami, T. Zheng, Y. Hu, S. Hwang, E. Stavitski, Y. Peng, J. Dynes, M. Gangisetty, D. Su, K. Attenkoferf, H. Wang, Isolated Ni single atoms in graphene nanosheets for high-performance CO₂ reduction, Energy Environ. Sci. 11 (2018) 893–903.

[3] C.S. Diercks, Y. Liu, K.E. Cordova, O.M. Yaghi, The role of reticular chemistry in the design of CO₂ reduction catalysts, Nat. Mater. 17 (2018) 301–307.

[4] D.R. Yang, L. Liu, Q. Zhang, Y. Shi, Y. Zhou, C. Liu, F.B. Wang, X.H. Xia, Importance of Au nanostructures in CO₂ electrochemical reduction reaction, Sci. Bull. 65 (2020) 796–802.

[5] Y.J. Zhang, V. Sethuraman, R. Michalsky, A.A. Peterson, Competition between CO₂ reduction and H₂ evolution on transition-metal electrocatalysts, ACS Catal. 4 (2014) 3742–3748.

[6] C. Jia, K. Dastafkan, W. Ren, W. Yang, C. Zhao, Carbon-based catalysts for electrochemical CO₂ reduction. Sustainable, Energy Fuels 3 (2019) 2890–2906.

[7] W. Ren, X. Tan, X. Chen, G. Zhang, K. Zhao, W. Yang, C. Jia, Y. Zhao, S.C. Smith, C. Zhao, Confinement of ionic liquids at single-Ni-sites boost electroreduction of CO₂ in aqueous electrolytes, ACS Catal. 10 (2020) 13171–13178.

[8] W. Yang, Y. Zhao, S. Chen, W. Ren, X. Chen, C. Jia, Z. Su, Y. Wang, C. Zhao, Defective indium/indium oxide heterostructures for highly selective carbon dioxide electrocatalysis, Inorg. Chem. 59 (2020) 12437–12444.

[9] Q. Sun, W. Ren, Y. Zhao, C. Zhao, Gram-scale synthesis of single-atom metal-N-CNT catalysts for highly efficient CO₂ electroreduction, Chem. Commun. 57 (2021) 1514–1517.

[10] W. Ren, X. Tan, J. Qu, S. Li, J. Li, X. Liu, S.P. Ringer, J.M. Cairney, K. Wang, S. C. Smith, C. Zhao, Isolated copper-tin atomic interfaces tuning electrocatalytic CO₂ conversion, Nat. Commun. 12 (2021) 1–8.

[11] W. Ren, X. Tan, W. Yang, C. Jia, S. Xu, K. Wang, S.C. Smith, C. Zhao, Isolated diatomic Ni-Fe metal-nitrogen sites for synergistic electroreduction of CO₂, Angew. Chem. Int. Ed. 58 (2019) 6972–6976.

[12] C. Jia, W. Ren, X. Chen, W. Yang, C. Zhao, (N, B) Dual heteroatom-doped hierarchical porous carbon framework for efficient electroreduction of carbon dioxide, ACS Sustain. Chem. Eng. 8 (2020) 6003–6010.

[13] W. Yang, S. Chen, W. Ren, Y. Zhao, X. Chen, C. Jia, J. Liu, C. Zhao, Nanostructured amalgams with tuneable silver-mercury bonding sites for selective electroreduction of carbon dioxide into formate and carbon monoxide, J. Mater. Chem. A 7 (2019) 15907–15912.

[14] Y. Zhao, X. Tan, W. Yang, C. Jia, X. Chen, W. Ren, S.C. Smith, C. Zhao, Surface reconstruction of ultrathin palladium nanosheets during electrocatalytic CO₂ reduction, Angew. Chem. Int. Ed. 59 (2020) 21493–21498.

[15] M. Valden, X. Lai, D.W. Goodman, Onset of catalytic activity of gold clusters ontitania with the appearance of nonmetallic properties, Science 281 (1998) 1647–1650.

[16] X. Sun, Y. Tuo, C. Ye, C. Chen, Q. Lu, G. Li, P. Jiang, S. Chen, P. Zhu, M. Ma, J. Zhang, J.H. Bitter, D. Wang, Y. Li, Phosphorus induced electron localization of single iron sites for boosted CO₂ electroreduction reaction, Angew. Chem. Int. Ed. 60 (2021) 23614–23618.

[17] S. Chen, B. Wang, J. Zhu, L. Wang, H. Ou, Z. Zhang, X. Liang, L. Zheng, L. Zhou, Y. Q. Su, D.S. Wang, Y. Li, Lewis acid site-promoted single-atomic Cu catalyzes electrochemical CO₂ methanation, Nano Lett. 21 (2021) 7325–7331.

[18] Y. Wang, X. Zheng, D. Wang, Design concept for electrocatalysts, Nano Res. (2021) 1–23.

[19] X. Zheng, P. Li, S. Dou, W. Sun, H. Pan, D. Wang, Y. Li, Non-carbon-supported single-atom site catalysts for electrocatalysis, Energy Environ. Sci. 14 (2021) 2809–2858.

[20] Q. Fan, P. Hou, C. Choi, T.S. Wu, S. Hong, F. Li, Y.L. Soo, P. Kang, Y. Jung, Z. Sun, Activation of Ni particles into single Ni-N atoms for efficient electrochemical reduction of CO₂, Adv. Energy Mater. 10 (2020) 1903068.

[21] Y. Zhang, X. Wang, S. Zheng, B. Yang, Z. Li, J. Lu, Q. Zhang, N.M. Adli, L. Lei, G. Wu, Y. Hou, Hierarchical cross-linked carbon aerogels with transition metal-nitrogen sites for highly efficient industrial-level CO₂ electroreduction, Adv. Funct. Mater. (2021) 2104377.

[22] M. Bourrez, F. Molton, S. Chardon-Noblat, A. Deronzier, [Mn (bipyridyl)(CO)₃Br]: an abundant metal carbonyl complex as efficient electrocatalyst for CO₂ reduction, Angew. Chem. Int. Ed. 50 (2011) 9903–9906.

[23] J.G. Chen, Electrochemical CO₂ reduction via low-valent nickel single-atom catalyst, Joule 2 (2018) 587–589.

[24] H. Coskun, A. Aljabour, P. De Luna, D. Farka, T. Greunz, D. Stifter, M. Kus, X. Zheng, M. Liu, A.W. Hassel, Biofunctionalized conductive polymers enable efficient CO₂ electroreduction, Sci. Adv. 3 (2017) e1700686.

[25] G.V. Last, M.T. Schmick, A review of major non-power-related carbon dioxide stream compositions, Environ. Earth Sci. 74 (2015) 1189–1198.

[26] M. Rumayor, A. Dominguez-Ramos, P. Perez, A. Irabien, A techno-economic evaluation approach to the electrochemical reduction of CO₂ for formic acid manufacture, J. CO₂ Util. 34 (2019) 490–499.

[27] F. Chang, G. Zhan, Z. Wu, Y. Duan, S. Shi, S. Zeng, X. Zhang, S. Zhang, Technoeconomic analysis and process design for CO₂ electroreduction to CO in ionic liquid electrolyte, ACS Sustain. Chem. Eng. 9 (2021) 9045–9052.

[28] B. Kim, S. Ma, H.R.M. Jhong, P.J.A. Kenis, Influence of dilute feed and pH on electrochemical reduction of CO₂ to CO on Ag in a continuous flow electrolyzer, Electrochim. Acta 166 (2015) 271–276.

[29] L. Jiao, W. Yang, G. Wan, R. Zhang, X. Zheng, H. Zhou, S.H. Yu, H.L. Jiang, Single-atom electrocatalysts from multivariate metal-organic frameworks for highly selective reduction of CO₂ at low pressures, Angew. Chem. Int. Ed. 59 (2020) 20589–20595.

[30] P. Hou, W. Song, X. Wang, Z. Hu, P. Kang, Well-defined single-atom cobalt catalyst for electrocatalytic flue gas CO₂ reduction, Small 16 (2020) 2001896.

[31] A.N. Soriano, B.T. Doma Jr, M.H. Li, Carbon dioxide solubility in some ionic liquids at moderate pressures, J. Taiwan Inst. Chem. Eng. 40 (2009) 387–393.

[32] E.K. Shin, B.C. Lee, High-pressure phase behavior of carbon dioxide with ionic liquids: 1-alkyl-3-methylimidazolium trifluoromethanesulfonate, J. Chem. Eng. Data 53 (2008) 2728–2734.

[33] S. Zhang, J. Zhang, Y. Zhang, Y. Deng, Nanoconfined ionic liquids, Chem. Rev. 117 (2017) 6755–6833.

[34] M. Asadi, B. Kumar, A. Behranginia, B.A. Rosen, A. Baskin, N. Repnin, D. Pisasale, P. Phillips, W. Zhu, R. Haasch, R.F. Klie, P. Kra´, J. Abiade, A. Salehi-Khojin, Robust carbon dioxide reduction on molybdenum disulphide edges, Nat. Commun. 5 (2014) 1–8.

[35] B.A. Rosen, A. Salehi-Khojin, M.R. Thorson, W. Zhu, D.T. Whipple, P.J. Kenis, R. I. Masel, Ionic liquid-mediated selective conversion of CO₂ to CO at low overpotentials, Science 334 (2011) 643–644.

[36] M. Galan-Sanchez, Functionalised ionic liquids, absorption solvents for CO₂ and olefin separation (Ph.D. thesis), (2008).

[37] S.P. Kelley, L.A. Flores, M.S. Shannon, J.E. Bara, R.D. Rogers, Understanding carbon dioxide solubility in ionic liquids by exploring the link with liquid clathrate formation, Chem. Eur. J. 23 (2017) 14332–14337.

[38] X. Zhang, Z. Liu, W. Wang, Screening of ionic liquids to capture CO₂ by COSMO-RS and experiments, AIChE J. 54 (2008) 2717–2728.

[39] H.B. Yang, S.F. Hung, S. Liu, K. Yuan, S. Miao, L. Zhang, X. Huang, H.Y. Wang, W. Cai, R. Chen, J. Gao, X. Yang, W. Chen, Y. Huang, H.M. Chen, C.M. Li, T. Zhang, B. Liu, Atomically dispersed Ni (I) as the active site for electrochemical CO₂ reduction, Nat. Energy 3 (2018) 140–147.

[40] L. Ramenskaya, E. Grishina, Intensification phenomenon of weak ionic interactions of 1-butyl-3-methylimidazolium hexafluorophosphate ionic liquid macro-dispersed in poly (methyl methacrylate): FTIR spectroscopic evidence, J. Mol. Liq. 218 (2016) 133–137.

[41] W. Sun, R.F. Gao, K. Jiao, Electrochemistry and electrocatalysis of a nafion/nano-CaCO₃/Hb film modified carbon ionic liquid electrode using BMIMPF₆ as binder, Electroanal. Int. J. Devoted Fundam. Pract. Asp. Electroanal. 19 (2007) 1368–1374.

[42] X. Li, W. Bi, M. Chen, Y. Sun, H. Ju, W. Yan, J. Zhu, X. Wu, W. Chu, C.Z. Wu, Y. Xie, Exclusive Ni-N₄ sites realize near-unity CO selectivity for electrochemical CO₂ reduction, J. Am. Chem. Soc. 139 (2017) 14889–14892.

[43] S.G. Han, D.D. Ma, S.H. Zhou, K. Zhang, W.B. Wei, Y. Du, X.T. Wu, Q. Xu, R. Zou, Q.L. Zhu, Fluorine-tuned single-atom catalysts with dense surface Ni-N₄ sites on ultrathin carbon nanosheets for efficient CO₂ electroreduction, Appl. Catal. B Environ. 283 (2021), 119591.

[44] C.M. Zhao, Y. Wang, Z.J. Li, W.X. Chen, Q. Xu, D.D. He, D.S. Xi, Q.H. Zhang, T. W. Yuan, Y.T. Qu, J. Yang, F.Y. Zhou, Z.K. Yang, X.Q. Wang, J. Wang, J. Luo, Y. F. Li, H.H. Duan, Y. Wu, Y.D. Li, Solid-diffusion synthesis of single-atom catalysts directly from bulk metal for efficient CO₂ reduction, Joule 3 (2019) 584–594.

[45] Y. Kim, W. Choi, J. Jang, K.P. Yoo, C. Lee, Solubility measurement and prediction of carbon dioxide in ionic liquids, Fluid Phase Equilib. 228 (2005) 439–445.

[46] J. Feng, S. Zeng, J. Feng, H. Dong, X. Zhang, CO₂ electroreduction in ionic liquids: a review, Chin. J. Chem. 36 (2018) 961–970.

[47] C. Cadena, J.L. Anthony, J.K. Shah, T.I. Morrow, J.F. Brennecke, E.J. Maginn, Why is CO₂ so soluble in imidazolium-based ionic liquids? J. Am. Chem. Soc. 126 (2004) 5300–5308.

[48] Z. Li, Q. Wang, D. Liu, B. Yang, X. Zhang, L. Lei, Ionic liquid-mediated electrochemical CO₂ reduction in a microbial electrolysis cell, Electrochem. Commun. 35 (2013) 91–93.

[49] B.A. Rosen, J.L. Haan, P. Mukherjee, B. Braunschweig, W. Zhu, A. Salehi-Khojin, D. D. Dlott, R.I. Masel, In situ spectroscopic examination of a low overpotential pathway for carbon dioxide conversion to carbon monoxide, J. Phys. Chem. C 116 (2012) 15307–15312.

[50] R. Chaplin, A.A. Wragg, Effects of process conditions and electrode material on reaction pathways for carbon dioxide electroreduction with particular reference to formate formation, J. Appl. Electrochem. 33 (2003) 1107–1123.

[51] X. Nie, M.R. Esopi, M.J. Janik, A. Asthagiri, Selectivity of CO₂ reduction on copper electrodes: the role of the kinetics of elementary steps, Angew. Chem. 125 (2013) 2519–2522.

[52] T. Zheng, K. Jiang, N. Ta, Y. Hu, J. Zeng, J. Liu, H. Wang, Large-scale and highly selective CO₂ electrocatalytic reduction on nickel single-atom catalyst, Joule 3 (2019) 265–278.

[53] K.R. Seddon, A. Stark, M.J. Torres, Influence of chloride, water, and organic solvents on the physical properties of ionic liquids, Pure Appl. Chem. 72 (2000) 2275–2287.

[54] D.S.H. Wong, J.P. Chen, J.M. Chang, C.H. Chou, Phase equilibria of water and ionic liquids [emim][PF₆] and [bmim][PF₆], Fluid Phase Equilib. 194 (2002) 1089–1095.

[55] D. Faggion Jr, W.D. Gonçalves, J. Dupont, CO₂ electroreduction in ionic liquids, Front. Chem. 7 (2019) 102.

[56] P. Yee, J.K. Shah, E.J. Maginn, State of hydrophobic and hydrophilic ionic liquids in aqueous solutions: are the ions fully dissociated? J. Phys. Chem. B 117 (2013) 12556–12566.

[57] R.L. Gardas, D.H. Dagade, J.A. Coutinho, K.J. Patil, Thermodynamic studies of ionic interactions in aqueous solutions of imidazolium-based ionic liquids [Emim] [Br] and [Bmim][Cl], J. Phys. Chem. B 112 (2008) 3380–3389.

[58] L. Cammarata, S. Kazarian, P. Salter, T. Welton, Phys. Chem. Chem. Phys. (2001).

[59] K. Mou, Z. Chen, X. Zhang, M. Jiao, X. Zhang, X. Ge, W. Zhang, L. Liu, Highly efficient electroreduction of CO₂ on nickel single-atom catalysts: atom trapping and nitrogen anchoring, Small 15 (2019) 1903668.